data

MDPI

Data Descriptor

In Vivo and In Vitro Electrochemical Impedance Spectroscopy of Acute and Chronic Intracranial Electrodes

Kyle P. O'Sullivan [1], Brian J. Philip [1], Jonathan L. Baker [2], John D. Rolston [3], Mark E. Orazem [4], Kevin J. Otto [5] and Christopher R. Butson [1,5,6,*]

[1] Department of Biomedical Engineering, University of Utah, 36 S Wasatch Dr, Salt Lake City, UT 84112, USA; kyle.osullivan@utah.edu (K.P.O.); brian.philip@utah.edu (B.J.P.)
[2] Brain and Mind Research Institute, Weill Cornell Medical College, 407 E 61st St, New York, NY 10065, USA; job2037@med.cornell.edu
[3] Brigham & Women's Hospital, Harvard Medical School, Boston, MA 02215, USA; jrolston@bwh.harvard.edu
[4] Department of Chemical Engineering, Herbert Wertheim College of Engineering, University of Florida, 1030 Center Drive, P.O. Box 116005, Gainesville, FL 32611-6005, USA; morazem@che.ufl.edu
[5] Department of Biomedical Engineering, Herbert Wertheim College of Engineering, University of Florida, 1275 Center Drive, NEB 363, P.O. Box 116131, Gainesville, FL 32611, USA; kevin.otto@bme.ufl.edu
[6] Norman Fixel Institute for Neurological Diseases, University of Florida, 3009 Williston Road, Gainesville, FL 32608, USA
* Correspondence: butsonc@ufl.edu

Abstract: Invasive intracranial electrodes are used in both clinical and research applications for recording and stimulation of brain tissue, providing essential data in acute and chronic contexts. The impedance characteristics of the electrode–tissue interface (ETI) evolve over time and can change dramatically relative to pre-implantation baseline. Understanding how ETI properties contribute to the recording and stimulation characteristics of an electrode can provide valuable insights for users who often do not have access to complex impedance characterizations of their devices. In contrast to the typical method of characterizing electrical impedance at a single frequency, we demonstrate a method for using electrochemical impedance spectroscopy (EIS) to investigate complex characteristics of the ETI of several commonly used acute and chronic electrodes. We also describe precise modeling strategies for verifying the accuracy of our instrumentation and understanding device–solution interactions, both in vivo and in vitro. Included with this publication is a dataset containing both in vitro and in vivo device characterizations, as well as some examples of modeling and error structure analysis results. These data can be used for more detailed interpretation of neural recordings performed on common electrode types, providing a more complete picture of their properties than is often available to users.

Dataset: Data discussed here can be found on the Dryad repository at the following link: https://doi.org/10.5061/dryad.8931zcrvw, accessed on 9 April 2024.

Keywords: electrochemical impedance spectroscopy; intracranial electrodes; in vivo; in vitro

Citation: O'Sullivan, K.P.; Philip, B.J.; Baker, J.L.; Rolston, J.D.; Orazem, M.E.; Otto, K.J.; Butson, C.R. In Vivo and In Vitro Electrochemical Impedance Spectroscopy of Acute and Chronic Intracranial Electrodes. *Data* **2024**, *9*, 78. https://doi.org/10.3390/data9060078

Academic Editor: Pufeng Du

Received: 10 April 2024
Revised: 14 May 2024
Accepted: 3 June 2024
Published: 6 June 2024

1. Summary

Intracranial electrodes are essential for recording brain activity and delivering therapeutic stimulation, with many uses in research and clinical settings. Whether they are used chronically or acutely, these devices develop complex interactions at the electrode–tissue interface (ETI) that change over time scales ranging from seconds to years. Understanding these interactions can provide important insights regarding the interpretation of neural recordings, estimation of the effects of stimulation, and management of closed-loop neuromodulation systems [1–4].

In typical applications, the properties of the ETI are characterized by measuring electrode impedance at a single frequency, usually with an instrument like the Bak Electrode Impedance Tester (Bak Electronics Inc., Umatilla, FL, USA). With this instrument, measurements are performed by emitting a 1 kHz sinusoidal current with an amplitude typically less than 30 nA. The system is capable of making measurements in the zero to five MOhm range. Such data are useful for verifying electrode continuity and identifying simple changes in the interface over time. This method of analysis has informed past studies of ETI changes in response to chronic foreign-body reactions [5,6] and is used in clinical applications to check device continuity and to identify connection failures. However, characterizing impedance over a wider spectrum of frequencies can provide more detailed information about the properties of the ETI, especially when the cutoff frequency and impedance range over the frequencies of interest is unknown.

In many areas of neuromodulation, there are new challenges in determining how energy crosses the ETI. During recording, users are often faced with assessing neural signals in which the features are not yet well understood, and these features can vary across a wide range of frequencies (for example, local field potentials). There is also a need to understand how stimulation waveforms are modified by the electrical properties of the ETI to better predict how charge will be delivered to tissue. In these cases, it is beneficial to determine whether changes in recording signals are due to evolution of the electrode-tissue interface or to alterations in the underlying neurophysiology. The dataset provided alongside this data descriptor presents a level of detail that is far greater than what most manufacturers provide to users and is greater than what can be discerned from a single frequency impedance measurement.

Electrochemical impedance spectroscopy (EIS) is a method for characterizing the complex impedance characteristics of an ETI over a range of frequencies. The measurement may be potentiostatic, in which a sinusoidal potential is superposed on a fixed potential, or it may be galvanostatic, in which a modulated current is superposed on a fixed current. The potential of a working electrode is measured against either a combined counter/reference electrode (Figure 1A) or a separate counter and reference (Figure 1B). In a three-electrode system, current passes between the working electrode and the counter electrode, and the reference electrode does not draw current but is used to sense potential.

EIS provides insights into the specific electrochemical processes occurring near an electrode. For instance, analyses of complex impedance can indicate the presence of capacitive and/or faradaic processes, estimations of material diffusion and charge distribution, and other frequency-dependent interface properties unknowable from single-frequency characterization. In a biotic–abiotic interface, this information is useful for separating the influence of implant properties from that of tissue responses after implantation. EIS measurements of the ETI have a demonstrated correlation with tissue properties [7–11], which can inform modeling of tissue and device behavior that may aid in the interpretation of recordings [12] and in the administration of stimulation pulses [13].

EIS can provide many useful insights regarding the ETI and its properties, but direct examination of raw EIS spectra may contain ambiguities. It is therefore useful to develop models to interpret these data by accounting for the known properties of the system that is being examined and to verify an acceptable signal-to-noise ratio (SNR) using an error-modeling system [14]. Measurement error can be further reduced by carefully controlling the conditions under which recordings are acquired and compared.

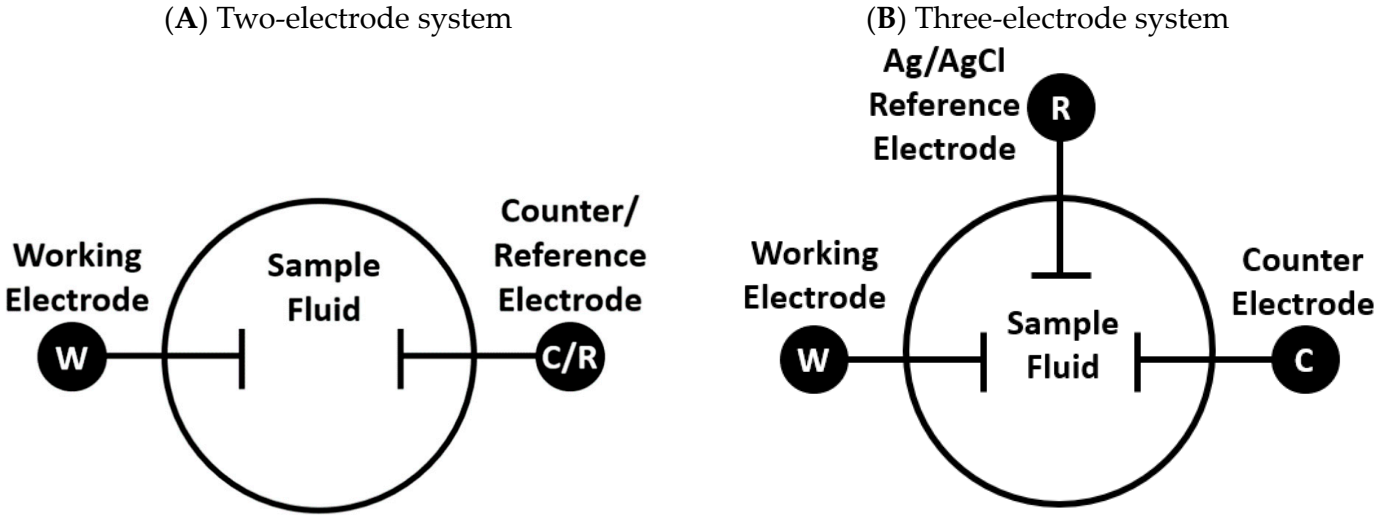

Figure 1. A simple representation of the two electrode configurations used in our data collection. (**A**) depicts a 2-electrode system where the working electrode (W) is the device being measured, and the combined counter/reference electrode (C/R) acts as a sink. The (C/R) electrodes used included platinum foil, platinum wire, and a titanium screw. (**B**) depicts the preferred 3-electrode configuration, with the reference and counter electrodes separated. Here, the counter electrode consisted of the foil, wire, or screw described above, with the reference electrode (R) consisting of silver/silver chloride.

Review articles have been written which provide guidance on the application of impedance spectroscopy for biomedical applications, but these do not provide sample data. One previous study [15] suggested a simplified model for the electrode–electrolyte interface that accounts for ohmic resistance in series with a parallel combination of a constant phase element (CPE) and a resistance. They argued that mass transfer was unimportant for their system. Critically, their model for a CPE was $Z = \frac{1}{(j\omega Q)^n}$, which yields values for Q that do not scale properly with the electrode's surface area. Previous work has also failed to account for the error structure of impedance measurements [16–18].

Several review papers have been written recently that do address the error structure of impedance measurements, but these do not address application to biological systems. One study [19] emphasized that "interpretation of impedance measurements requires both a model that accounts for the chemistry and physics of the system under study and the error structure of the data". The authors demonstrated application of a measurement model to assess stochastic and bias errors. The need for error analysis is likewise emphasized by Vivier and Orazem [20], who provide a step-by-step tutorial for impedance data analysis. These papers also do not provide sample data.

The goal of this data acquisition was to provide electrical impedance properties of several intracranial research and clinical electrodes, both to assess their electrochemical characteristics and to demonstrate the utility of a carefully controlled recording and modeling process. These full-spectrum data go beyond the commonly used impedance at 1 kHz and single-frequency impedance testing built into clinical pulse generator systems. We also provide error analysis approaches developed by the Orazem group. These data may aid in differentiating electrode properties from those of tissue, with potential for use in filtering or result interpretation, as well as in assessment of variability and manufacturing consistency within an electrode. The effects of design differences, between-contact variability, solution properties, environmental conditions, electrode setup, and return electrode materials are discussed, and comparisons between these conditions may provide useful insights when interpreting data collected under constrained conditions, such as is common in vivo. All data are provided in a hosted repository along with examples of fitted models and error structure analysis.

2. Data Description

Data discussed in this study are stored on the Dryad data repository (https://doi.org/10.5061/dryad.8931zcrvw, accessed on 9 April 2024) [21]. Data from EIS scans, including frequencies and complex, real, and imaginary impedances, are provided in the comma-separated value (.CSV) format, as well as the proprietary PalmSens *.pssession format, for use by those with similar PalmSens instruments. In addition, for select portions of the included data, we have performed modeling and error regression analysis. These items are provided both in the Measurement Model software format and in .CSV. Data are organized according to the electrode model used, labeled by manufacturer and form factor.

Files in this dataset are organized into folders and subfolders based on electrode type and whether the data were recorded in vitro or in vivo. Parent folders in our file directory are named for the model of electrode used, with an additional folder containing our fitted model data ("fitted model example") and another folder containing the single-frequency impedance data from a Bak impedance tester, as well as the interpolated 1 kHz values created using PalmSens data. Subfolders within each parent electrode folder are as follows. For electrodes measured using solutions of varying conductivity, data are organized into folders based on the solution used (CSF for cerebrospinal fluid, GM for gray matter, PBS for phosphate-buffered saline, and WM for white matter; see glossary of terms in the Readme file). For electrodes with both in vivo and in vitro data, subfolders are organized into those categories. Within the in vitro folder, data are organized into two- and three-electrode subfolders. Within the in vivo folder, data are further sorted into folders for Animal 1 and Animal 2. File names for each dataset specify details about how the recording was performed, including what counter/reference electrode was used, the temperature of the solution, and the type of solution. When not otherwise noted, the fluid used in in vitro measurements was phosphate-buffered saline (PBS). Note that temperature measurements were accurate to within a tenth of a degree.

Data included here are encoded in both *.csv and *.pssession formats. The *.csv files include columns for frequency, negative phase angle, DC current, complex impedance, real component of impedance, negative imaginary component of impedance, and charge. This file type should be readable by many types of software. The included *.pssession files are a proprietary format used by our PalmSens4 Potentiostat instrument's corresponding software, PSTrace (https://www.PalmSens.com/software/ps-trace/ (accessed on 9 April 2024). These files may be useful to others who use PalmSens instruments and software. A Python script used to convert from the *.pssession file type to .csv format is also included and is described in the "Code Availability" (Section 2.2).

2.1. Data Utility

The EIS data presented here represent a broad range of clinical and experimental electrode form factors and can be used to create electrochemical models of these devices in vitro and in vivo. While single-frequency impedance measurement is often performed in clinical electrodes or lab settings for the purpose of continuity checks and verification of device function, full-spectrum EIS recordings are more rarely seen, and such data are not commonly provided by clinical device manufacturers. EIS is the gold standard method for characterizing device impedance and capturing frequency-dependent attributes of a device's performance, particularly frequencies of interest where neural activity is observed or stimulation is delivered. For researchers without access to the specialized equipment and methods required for robust EIS measurement, this dataset may serve as an invaluable tool for understanding relevant device characteristics and for fitting equivalent circuit models or creating finite element approximations of stimulation and recording.

For those with access to EIS measurement tools, the data and validation methods described herein can provide guidance for best practices in measurement and analysis, especially for biomedical engineers without extensive experience in the discipline of electrochemistry. Considerations such as counter or reference electrode material and surface area, number of electrodes used, temperature control, and stochastic error modeling are commonly discussed in electrochemical contexts but are often overlooked in applications of impedance measurement in biomedical engineering. We present a dataset collected under carefully controlled and clearly described conditions for comparison to future in vitro and in vivo EIS data and use in biophysical models. Such a dataset does not currently exist for use by biomedical engineers working with invasive electrodes and may provide a useful baseline for comparison to newly acquired datasets. Full-spectrum EIS data provide an in-depth understanding of how device hardware will influence charge transfer in neural engineering under relevant conditions that more common single-frequency characterizations cannot provide.

2.2. Code Availability

Data processed in this study were saved in the proprietary .pssession format by our PalmSens4 Potentiostat instrument. These files can be accessed using the software PSTrace version 5.9 or later (https://www.PalmSens.com/software/ps-trace/ (accessed on 9 April 2024)). Data are also included in the more accessible comma-separated values (.CSV) format, converted using a custom Python script included in our repository (possession_parser.py). This script was developed for Python version 3.8+ and requires the Pandas package version 1.1.1 or higher. Error structure analysis and weighted modeling of the data were performed using the Measurement Model software developed by Watson and Orazem, which is available at https://ecsarxiv.org/kze9x/ (accessed on 9 April 2024).

3. Methods

3.1. Electrochemical Impedance Spectroscopy

This technique involves measurement of an electrochemical interface by applying a sinusoidal voltage waveform at a range of frequencies. For potentiostatic modulation, a single perturbation amplitude is maintained across the frequency spectrum, typically lower than amplitudes used in biological stimulation. The frequency range chosen for these measurements was 10 Hz–100 kHz, with an amplitude of 0.01 V. Data were sampled at 39 frequency intervals across this spectrum. Using the complex impedance values obtained by our instrument, a fitted model was created to approximate the components of the biotic–abiotic interface. We visualized EIS spectra using Nyquist-style plots, where the real component of complex impedance is plotted on the x-axis and the imaginary component on the y-axis. There are many ways to represent these axes, but we chose the IUPAC standard [22], which denotes real impedance as Z' and imaginary impedance as Z''.

3.2. Animal Ethics Statement

The methods reported follow the ARRIVE guidelines (https://arriveguidelines.org/ (accessed on 9 April 2024)). All work was performed in strict accordance with the National Institutes of Health guidelines for the use of animals in research and under an approved protocol from the Weill Cornell Medical College Institutional Animal Care and Use Committee (IACUC). Animals were cared for by the Research Animal Resource Center (RARC) at Weill Cornell Medicine.

3.3. Data Collection

Data were primarily collected using a PalmSens4 Potentiostat instrument in electrochemical impedance spectroscopy mode, both in vitro and in vivo, in awake and behaving nonhuman primates (NHPs). NHP subjects included two adult male rhesus macaque monkeys chronically implanted (over 1 year implantation) with both penetrating deep brain stimulation (DBS) electrodes and surface-contact electrocorticography (ECoG) electrodes placed epidurally [23]. Measurements in vivo were performed only in 2-electrode mode and used a titanium screw or rod that was secured to within animal's cephalic implants as a return electrode. The titanium screw and rod were in contact with the dural surface. For in vitro measurements, a 2-electrode system was employed for direct comparison to typical in vivo data collection methods. A 3-electrode system, including an Ag/AgCl reference electrode, was also used in vitro to verify the reliability of the 2-electrode system. The PalmSens device was operated using battery power to isolate it from electrical line noise.

Sample fluids used in vitro included phosphate-buffered saline (PBS) at 1× concentration and artificial cerebrospinal fluid (aCSF). The sample fluid temperature was regulated to approximate biological conditions, specifically, NHP internal body temperature of approximately 37 °C. Temperature regulation was performed using a Gamry electrochemical flow-cell with a 1 L solution volume connected to a thermally regulated bath which circulated in an external jacket. Temperature measurements were verified to within plus or minus 0.1 °C using a Thermoworks Type T High Precision Thermocouple Meter with an immersion probe (Figure 2).

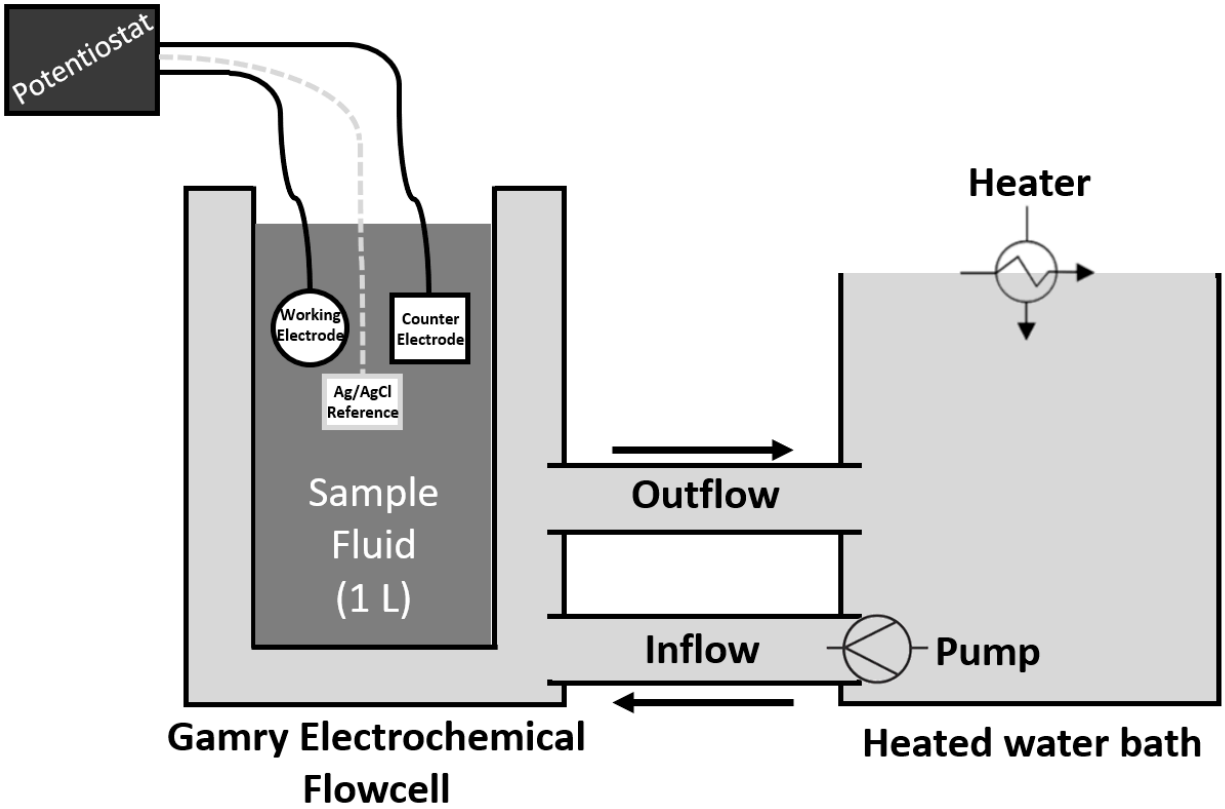

Figure 2. Diagram of the in vitro experimental setup. Electrodes for two-electrode or three-electrode EIS measurements were immersed in 1 L of sample fluid (dark gray), which was isolated from the temperature-regulation bath (light gray). Temperature-regulating water was circulated between a heated reservoir and the glass outer jacket of the Gamry Electrochemical Flowcell and did not make contact with the sample fluid. Note that items represented are not to scale.

Working electrodes included a selection of commercially available intracranial electrodes designed for both human and NHP applications. Electrodes used for in vivo measurements were chronically implanted, and connection to the PalmSens device was achieved via an external Omnetics connector. The in vivo counter electrode consisted of a titanium screw with a 61 mm^2 surface area for Animal 1 and a titanium rod of 1 mm diameter and 48 mm length, with approximately 1 mm in contact with brain tissue, for Animal 2, with the same approximate surface area in contact with the dura. Counter electrodes used in vitro included a titanium screw similar to that used in vivo, as well as platinum wire (7.5 cm length/0.5 mm diameter) and platinum foil (625 mm^2). When a 3-electrode measurement system was applied, the "reference" consisted of a silver/silver chloride (Ag/AgCl) electrode, as is typically employed in nonbiological EIS applications.

For comparison to standard methods of electrode impedance verification, in vitro measurements were also performed using a Bak Electrode Impedance Tester calibrated with a 1 kOhm resistor. In this setup, impedance was computed between two contacts: a working electrode and a counter electrode.

3.4. Setup and Solution Preparation

Gray matter, white matter, and cerebrospinal fluid have been measured at a range of conductivity values (1.71 $\pm$ 0.30 S/m for cerebrospinal fluid, 0.46 $\pm$ 0.23 S/m for gray matter, 0.22 $\pm$ 0.17 S/m for white matter) [24]. We used gray and white matter conductivities of 0.33 and 0.142 S/m, respectively [25]. The required NaCl concentration to mimic gray and white matter solutions was found by measuring the conductivity of dissolved NaCl at intervals of 0.5 g/L at 37 °C $\pm$ 0.1 °C until the measured conductivity was greater than 0.33 S/m. Laboratory-grade NaCl (Thermo Fisher Scientific, Waltham, MA, USA) was added between intervals and mixed using a vortex at 300 rpm until clear. A line fit to these conductivity values was used to find salt concentrations that approximated the conductivity of gray and white matter. The aCSF was made using 12.6 mM NaCl, 3 mM KCl, 26 mM $NaHCO_3$, 1.4 mM NaH_2PO_4, 10 mM Glucose, 2 mM $CaCl_2$, and 2 mM $MgSO_4$, with an osmolarity of 306 mOsm/L and pH of 7.36.

For in vitro recordings, electrodes were suspended in solution with all contacts fully immersed in electrolyte without touching the glass side walls. EIS was measured using the Bak Electrode Impedance Tester and the PalmSens device. The PalmSens device delivered 10 Hz–10 kHz, 0.1 nA–100 µAmps. The electrodes included in this comparison between the Bak and PalmSens instruments were the AdTech Depth, AdTech Strip, AdTech Grid, Dixi Depth, NeuroPace Depth, NeuroPace Strip, and AdTech Behnke-Fried. To facilitate experimental determination of the stochastic error structure, trials were repeated 3$\times$ per electrode.

For in vivo recordings, the exposed distal end of the DBS or ECoG electrode was accessed, and a titanium screw or rod mounted in the NHP cephalic implant served as a combined counter/reference electrode. A PalmSens MUX8/R2 Multiplexer facilitated switching between channels of the working electrode, with three scans performed per channel to facilitate error regression (Figure 3).

Electrodes measured in this dataset include an Ad-Tech ECoG strip and grid, Ad-Tech Depth, BF series epilepsy and SEEG electrodes, CorTec Fetz spinal cord ECoG and Micro Square, Dixi Depth, FHC Inc. Microelectrode, Heraeus segmented nonhuman primate deep brain stimulation electrode, Medtronic SenSight, NeuroPace ECoG strip and depth electrodes, NuMed DBS, and a Thomas Recording 3D Heptrode (Table 1).

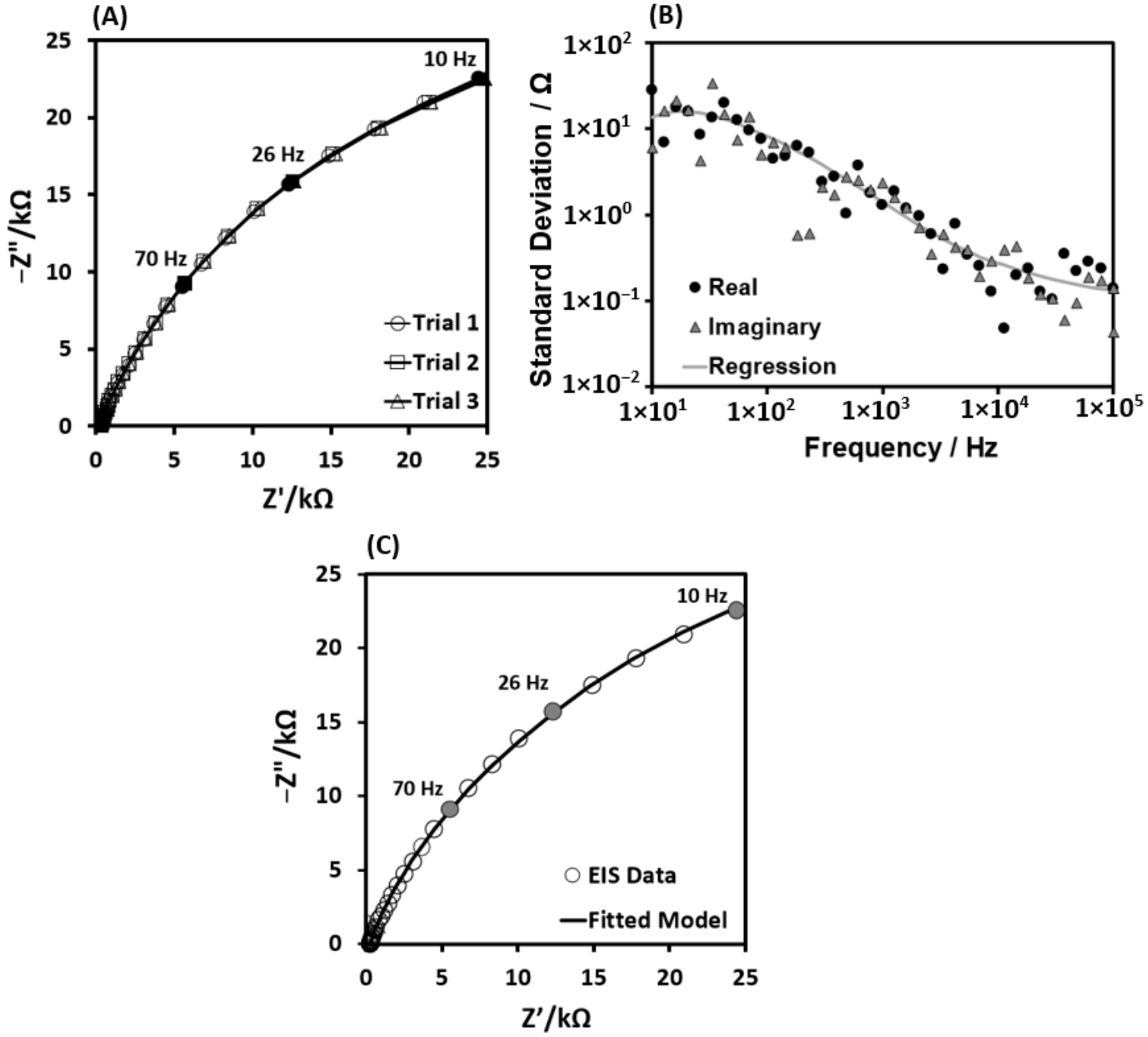

Figure 3. A depiction of the steps used for our example of weighted regression of 3 EIS scans of a single electrode contact. (**A**) Nyquist plot showing three repetitions of an EIS scan on the same electrode contact. These data were fit using the Measurement Model software, producing the output available in the "Fitted model example" folder. (**B**) Plot showing an example error regression model, representing the standard deviations of the real and imaginary components of complex impedance as evaluated using the measurement model parameters contained in "fitted model example". Variables were added or removed from the standard error model equation (Equation (1)) as necessary to ensure the best fit for each case. A good fit ensures compliance with Kramers–Kronig relations and indicates a good signal-to-noise ratio. Data shown here were recorded from a single segment of a Heraeus nonhuman primate segmented deep brain stimulation lead using two electrodes, with 625 mm^2 platinum foil as a counter electrode. Both electrodes were immersed in temperature-controlled PBS solution at 37 °C. (**C**) Example Nyquist plot following custom model-fitting. The above data were fit using Equation (2), with regression weighted by the error analysis shown in Figure 3B. The line represents the fitted model, and the points represent the measured data.

Table 1. Description of electrodes used in our dataset, including form factor, dimensions of contacts, approximate surface areas, and contact materials.

Electrode Name	Form Factor	Contact Dimensions	Contact Surface Area	Material
Adtech BF BF08R-SP05X-000	8 cylindrical contacts	1.57 mm contact height, 1.28 mm contact diameter, 2 mm spacing between contacts	8.89 mm^2	90% Pt/10% Ir
Adtech depth RD10R-SP05X-000	10 cylindrical contacts	2.29 mm contact height, 0.86 mm contact diameter, 2 mm spacing between contacts	7.35 mm^2	90% Pt/10% Ir
Adtech Grid FG64C-SP10X-0CB	64 contact grid w/circular contacts	4 mm contact diameter, 10 mm spacing between contact centers	2.3 mm^2	90% Pt/10% Ir
Adtech strip IS04R-SP10X-000	4 circular contacts, surface electrode	4 mm contact diameter, 10 mm spacing between contact centers	2.3 mm^2	90% Pt/10% Ir
CorTec Fetz Spinal Cord ECoG	8-contact surface strip with circular contacts	0.6 mm diameter, center-center spacing between 2 and 3 mm	0.28 mm^2	90% Pt/10% Ir
CorTec Micro Square ECoG	32 contact surface grid with circular contacts	1 mm contact diameter, centers spaced 4.25 mm apart	0.79 mm^2	90% Pt/10% Ir
Dixi Depth D08-15CM	8 cylindrical contacts in two groups of four	2 mm height, 0.8 mm diameter, 1.5 mm spacing between contacts, 15 mm spacing between groups	6 mm^2	90% Pt/10% Ir
FHC Microelectrode	Single micro contact extended from a canula	125 micron diameter platinum/iridium wire, extends up to 0.5mm from canula	not specified by manufacturer	90% Pt/10% IrPlatinum black coating
Hereaus NHP DBS	Segmented 12-channel DBS, 4 contact rings with 3 contacts per ring	Contacts are segmented from cylinders with 0.8 mm diameter, 0.5 mm height. 104.49° of arc per segment, 0.51 mm spacing between rings	0.37 mm^2	90% Pt/10% Ir
MDT SenSight	DBS lead with 8 contacts in a 1-3-3-1 configuration (first and fourth are solid cylinders, middle two are segmented into 3 contacts each)	1.5 mm cylinder height, 1.36 mm diameter, 0.5 mm spacing between	9.31 mm^2	90% Pt/10% Ir
NeuroPace Depth DL-330-3.5	4 cylindrical contacts, depth electrode	1.27 mm diameter, 2 mm hheight	10 mm^2	90% Pt/10% Ir
NeuroPace strip CL-335-10	4 circular contacts, surface electrode	3.175 mm diameter	8 mm^2	90% Pt/10% Ir
NuMED for children DBS	4 cylindrical contacts, depth electrode	0.8 mm diameter, 0.5 mm height	2.26 mm^2	90% Pt/10% Ir
Thomas Recording 3D Heptrode	7 contacts exposed on electrode tip	Fiber with 100 micron diameter, 6 contacts approx. 50 microns in length and 10 microns in width on tip taper, one at tip terminus approx. 30 microns in length	approx. 3.6 mm^2 total	platinum/tungsten

3.5. Data Analysis

EIS spectra were measured in three repetitions for each device to allow for error modeling and regression analysis. This analysis quantifies the stochastic error structure for the data; this aids in identifying the signal-to-noise characteristics of our measurement instrument, facilitates regression analysis by providing a weighting strategy based on measurement characteristics, and provides meaning to the weighted chi-squared statistic which has a value near the degree of freedom for a successful regression. The measurement model used for error analysis also may be used to identify the frequency range of our measurements that is consistent with Kramers–Kronig relations, which verifies that the real and imaginary parts of our complex impedance values are consistent with a linear, stable measurement system. Knowledge of the error structure of the data is an essential part of interpretation.

While both a process model and measurement model can be used to fit the present data, note that the measurement model described below presents several advantages. When a process model fails to fit the data spectrum, the poor fit might be attributed to an incorrect or inadequate model, poor initial guesses, or lack of consistency of the data with Kramers–Kronig relations. The measurement model described below has been shown to provide a good fit to any EIS spectrum that is consistent with Kramers–Kronig relations and provides a reliable and systematic procedure for estimating initial guesses during the fitting process. The standard deviation for the stochastic error structure is used to weight regressions and determine fit quality. Only the frequency range of the impedance spectrum that shows Kramers–Kronig consistency is used for regression of the interpretation model, thus eliminating the influence of confounding factors such as nonstationary phenomena and instrument artifacts.

This model fitting and error structure analysis was performed using the Measurement Model software developed by Watson and Orazem [26].

The procedure followed a series of steps:

1. The Voigt measurement model,

$$Z = R_e + \sum_{k=1}^{N} \frac{R_k}{1 + j\omega\tau_k} \tag{1}$$

was fitted to each replicate spectrum for a given electrode and operating condition. In Equation (1), Z is the impedance, R_e is the ohmic resistance, R_k is the resistance for element k, $t_k = R_k C_k$ is the time constant for element k, and C_k is the capacitance for element k. The standard deviation of the residual errors was used as an estimate of the standard deviation of the stochastic errors. Ref. [27] have shown that the standard deviation obtained in this manner is independent of the measurement model used, and [28] have shown that the statistical characteristics of the error structure obtained by this method agree with propagation of time-domain noise through an electrochemical cell and Fourier-analysis-based instrumentation. The measurement model provided a way to filter the bias errors that confound replication of impedance spectra, which can take minutes to complete.

2. The standard deviations so obtained are strong functions of frequency. An empirical model,

$$\sigma = \sigma_r = \sigma_j = \alpha\left|Z_j\right| + \beta\left|Z_r\right| + \gamma|Z|^2 + \delta \tag{2}$$

was fitted to standard deviations obtained by the measurement model analysis. Equation (2) provided a convenient way to weight regressions by the stochastic error structure.

3. Subsequent regressions were weighted by $1/\sigma^2$, where σ was obtained from Equation (2).

The consistency of the spectra with the Kramers–Kronig relations was confirmed by fitting Equation (1) to the spectra using either a weighted complex nonlinear regression or regression to the real or imaginary part of the impedance. As Equation (1) satisfies the Kramers–Kronig relations, the ability to provide a statistically satisfactory fit of the measurement model to a spectrum demonstrates that the data also satisfy the Kramers–Kronig relations. Error analysis by use of a general measurement model is preferred to use of a process model that accounts specifically for the chemistry and physics of the system under study because the measurement model satisfies the Kramers–Kronig relations and has been shown to provide a statistically significant fit to data that satisfy the Kramers–Kronig [19] relations.

While most process models also satisfy the Kramers–Kronig relations [29,30], an inability of such a model to fit a spectrum may be caused by use of an incorrect or inadequate model, poor initial guesses for model parameters, or inconsistency of the data with Kramers–Kronig relations. Use of the measurement model, for which a systematic method exists to identify initial parameter estimates, reduces the ambiguity associated with relying on process model fits to assess consistency with the Kramers–Kronig relations.

Sample replicated measurements and the standard deviations for real and imaginary parts of the impedance are shown in Figure 3. The line in this figure represents the fit of Equation (2) to the standard deviations. The analysis described above verified that the PalmSens instrument's measurements provided an acceptable signal-to-noise ratio (SNR). In addition, the data were found to be consistent with the Kramers–Kronig relations.

4. User Notes

Interpretation and reuse of EIS data may be aided by application of the process modeling described below. Other considerations include the type of electrodes and setup used for EIS data collection; differences in these factors are important to note when comparing datasets, especially when comparing in vivo and in vitro data.

4.1. Data Validation—Process Model

A process model was developed to account for the faradaic reactions that take place at the electrode–electrolyte interface. The method for model development was described by Vivier and Orazem [20]. The cathodic reaction was presumed to be reduction of oxygen, and the corresponding cathodic impedance was expressed as:

$$Z_c = R_{t,c} + R^*_{d,c} Z_{d,c} \tag{3}$$

where $R_{t,c}$ is the charge-transfer resistance accounting for the kinetics of the reaction, $Z_{d,c}$ is the diffusion impedance given as:

$$Z_{d,c} = \frac{1}{\sqrt{j\omega}} \tag{4}$$

and $R^*_{d,c}$ is the diffusion resistance that incorporates the square root of the diffusion time constant, i.e.,:

$$R^*_{d,c} = R_{d,c} / \sqrt{\tau_{d,c}} \tag{5}$$

where R_d has units of $\mathrm{Wcm^2}$, and $R^*_{d,c}$ has units of $\mathrm{Wcm^2 s^{-1/2}}$. As the electrodes were relatively inert, the anodic reaction was presumed to be oxygen evolution where:

$$Z_a = R_{t,a} \tag{6}$$

The electrode was assumed to behave as an imperfect capacitor for which a constant-phase-element behavior was assumed. Thus,

$$Z_{cpe} = \frac{1}{(j\omega)^{\alpha} Q} \tag{7}$$

The complete model for the system was given as:

$$Z = R_e + \frac{1}{1/Z_a + 1/Z_c + (j\omega)^{\alpha} Q} \tag{8}$$

A Levenberg–Marquardt regression was used to fit the model to the data using the Python scripting module. Parameters were retained in the model only if the 95.4% confidence interval, based on the calculated standard deviation of the parameter estimate, did not include zero. Sample results are presented in the dataset in the folder "Fitted model example", for which the parameter $R_{t,c}$ was removed from the model because it was not statistically significant.

Typical results are presented in Table 2. The electrode was a single contact (0.37 mm^2 surface area) of a segmented deep brain stimulation lead, platinum–iridium alloy (90% Pt, 10% Ir) immersed in phosphate-buffered saline heated to primate body temperature (37 °C). The contact shape was roughly one-third of a section of a cylinder, and the exposed face was a curved rectangle. Two-electrode and three-electrode results are presented. As expected, the ohmic resistance for the two-electrode setup was larger than that for the three-electrode setup. The χ^2/n statistic is a weighted value where the weighting was the inverse of the experimentally measured variance of the measurement. An ideal value would have a value close to unity, i.e., $\frac{\chi 2}{\nu} = 1 + \sqrt{\frac{2}{\nu}}$. The values show a good fit but suggest that improvement may be possible. The other variables—R_d, $R_{t,a}$, and Q—show some variability, which can be attributed to small changes in electrode properties. The Brug formula [31],

$$C = Q^{1/\alpha} \, R_e^{(1-\alpha)/\alpha} \tag{9}$$

developed for CPEs characterized by a surface distribution of time constants, yielded values of 19.3 mF/cm^2 for both the two-electrode and three-electrode configurations. This value is well within the usual 10–50 mF/cm^2 range expected for a double layer.

Table 2. Results for regression of the process model to the data presented in Figure 3. Note that resistances and Q values have been scaled for electrode surface area.

Variable	Two-Electrode	Three-Electrode
R_e, Ω	10.57 ± 0.02	9.42 ± 0.02
$R_{t,a}$, kΩ	4.0 ± 0.2	2.3 ± 0.1
R_d, kΩ	19.2 ± 0.6	18.3 ± 1.1
Q, $\mu F/s^{1-\alpha}$	7.0541 ± 0.2270	7.1622 ± 0.4054
α	0.8801 ± 0.0028	0.8797 ± 0.0047
χ^2/υ	54	278
C, $\mu F/cm^2$	19.3	19.3

4.2. Comparison of Two- and Three-Electrode Data

All devices studied were measured using both two-electrode and three-electrode configurations (Figure 1) to evaluate the utility of the in vivo two-electrode system in comparison to more accurate methods typically applied in vitro. Differences between the two-electrode and three-electrode measurements performed in vitro were present, with two-electrode spectra typically representing a similar morphology to three-electrode equivalents

but with variation in the precise measured values (Figure 4). This difference suggests that whereas the two-electrode system used in vivo produces useful insights into the behavior of an ETI and its frequency-dependent properties, some compromise of precision is necessary. Note that the data in Figure 4 are presented both in their raw form (Figure 4A) and after correction for ohmic resistance [32] (Figure 4B) using Equations (10) and (11). This correction is possible when modeling provides an accurate estimate of electrolyte resistance R_e and provides the possibility of gleaning additional information regarding constant phase element (CPE) behaviors that may be obscured in a traditional Bode plot presentation [32].

$$\left|Z_{adj}\right| = \sqrt{(Z_r - R_e)^2 + {Z_i}^2} \tag{10}$$

$$\Phi_{adj} = \tan^{-1}\left(\frac{Z_i}{Z_r - R_e}\right) \tag{11}$$

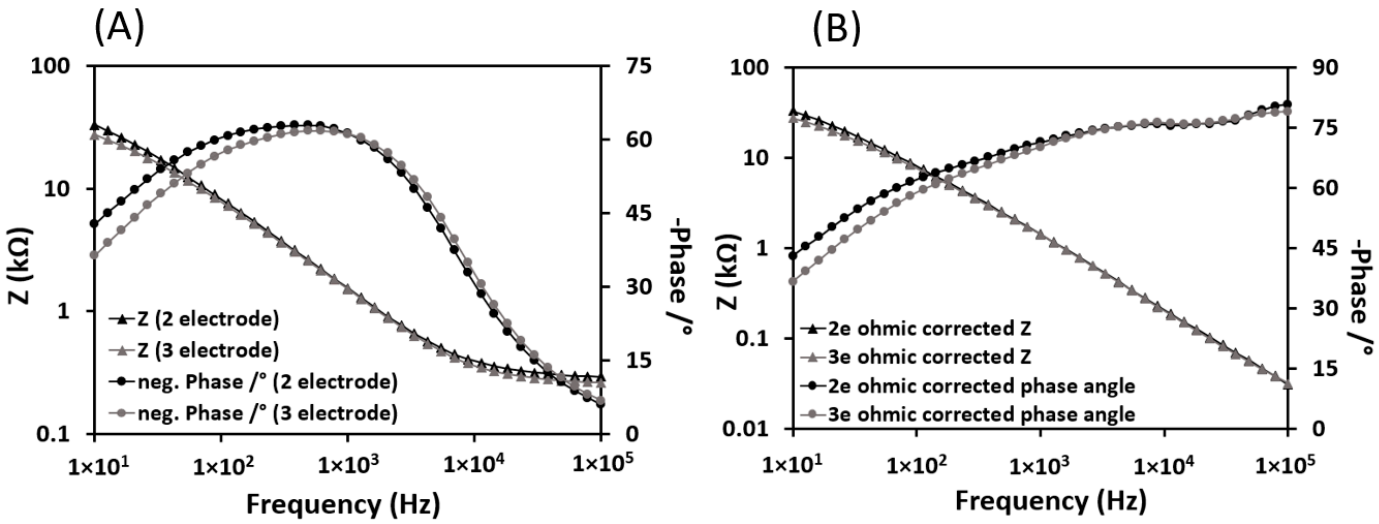

Figure 4. Comparison of complex impedance measurements (Z) and phase angle vs. frequency for two-electrode and three-electrode measurements of the same electrode contact (Heraeus segmented lead) in saline solution. Note that the plots' morphology is consistent, while specific measured values deviate, particularly at lower frequencies. (**A**) Depicts these data uncorrected, while (**B**) depicts these data when corrected for ohmic resistance (Equations (9) and (10)).

4.3. Comparison of In Vivo and In Vitro Data

Data were collected in vivo from two adult male rhesus macaque NHPs. DBS and ECOG electrodes chronically implanted in their cortices were tested. Identical electrode models were tested in vitro in a solution approximating biological conductivity and temperature. Given the length of implantation for each device, a pronounced "tissue component" was expected, typically presenting as a semicircular "arc" on a Nyquist plot (Figure 5) [12]. This arc indicates the changes in electrode–tissue interface dynamics that accompany the brain's fibrous encapsulation of a device, attributable to the complex dielectric properties of the tissue [33], which tends to become more pronounced as fibrous encapsulation worsens. Tissue component contributions were observed in all in vivo EIS data collected, disrupting the comparatively linear spectra observed in vitro for similar devices. Note that the high-frequency components of the impedance response in Figure 5 present a similar morphology to the spectra measured in vitro, with deviations becoming more pronounced at lower frequencies.

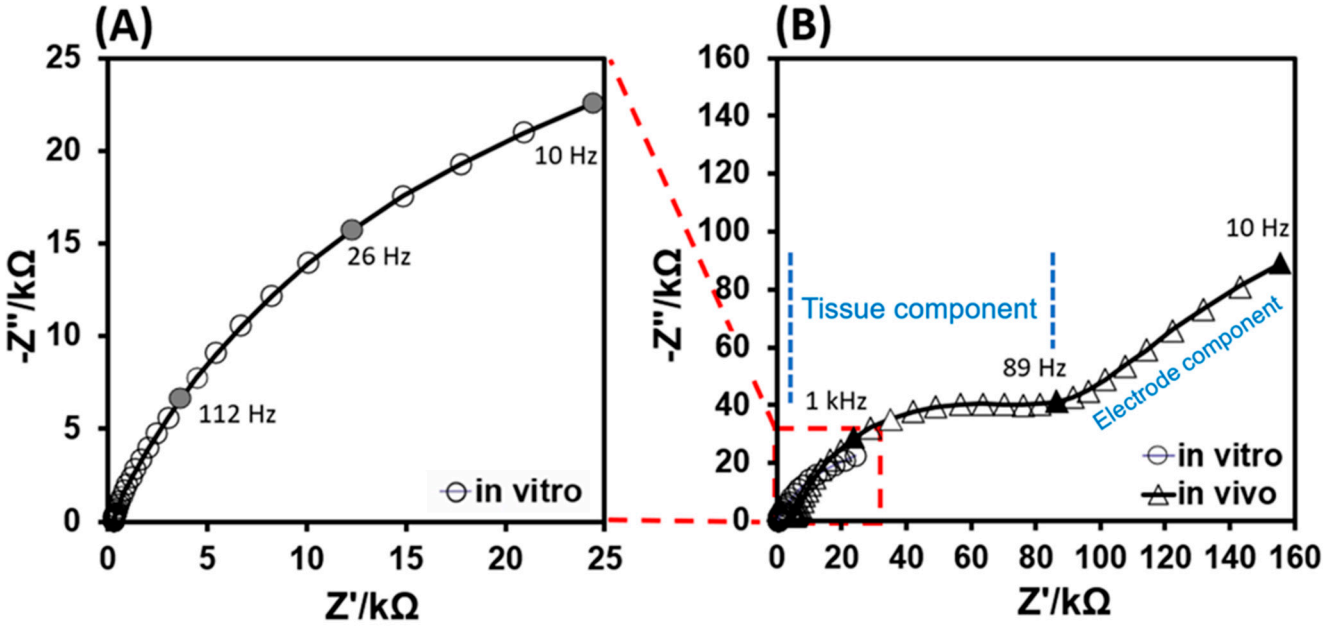

Figure 5. Comparison of EIS spectra collected from the same model of electrode (Heraeus NHP segmented lead). Both in vitro and in vivo data are shown in panel (**B**), while in vitro data are shown in isolation in the inset panel (**A**). Note the inflection point visible in the in vivo spectra near 89 Hz, highlighting the presence of dielectric properties of the tissue surrounding the electrode. The high-frequency end of the EIS spectra thus forms the semicircular "tissue component" (labeled in blue, between the dashed lines). The remaining, comparatively linear portion of the EIS spectra at lower frequencies is labeled as the "electrode component". In vivo data shown in this figure are from channel one in the file "animal1_dbsLead_Ch1-12_tr3_in_vivo_5_17" in our dataset, recorded over 1 year post-implantation in Animal 1.

4.4. Compliance of PalmSens Data with BAK

Single-frequency impedance characterizations are a common method for verifying electrode continuity and functionality, both as a built-in manufacturer function check and as performed by external instruments. One common device, the Bak Impedance Analyzer (Bak Electronics Inc., Umatilla, FL, USA), uses a 1 kHz frequency to check impedance response. To verify compliance and consistency with measurements performed by the PalmSens4 Potentiostat in EIS mode, we performed tests using both instruments on a subset of electrodes (Figure 6). Note that the results provided by the Bak instrument demonstrated good compliance with the EIS spectra produced by the PalmSens device. Figure 6 illustrates the utility of EIS in identifying a wider spectrum of frequency-dependent behaviors of the electrode–tissue interface that are not captured by the narrower information provided in a single-frequency measurement.

4.5. Impact of Temperature Regulation

One aspect of electrochemical impedance characterization often overlooked in biological comparisons is temperature control. To highlight the impact of environmental conditions on the response of an electrode–substrate interface, we tested an electrode at room temperature and at body temperature under controlled conditions (Figure 7). These results demonstrate that impedance acts as a function of temperature and is an important consideration when comparing in vitro electrode properties to in vivo data.

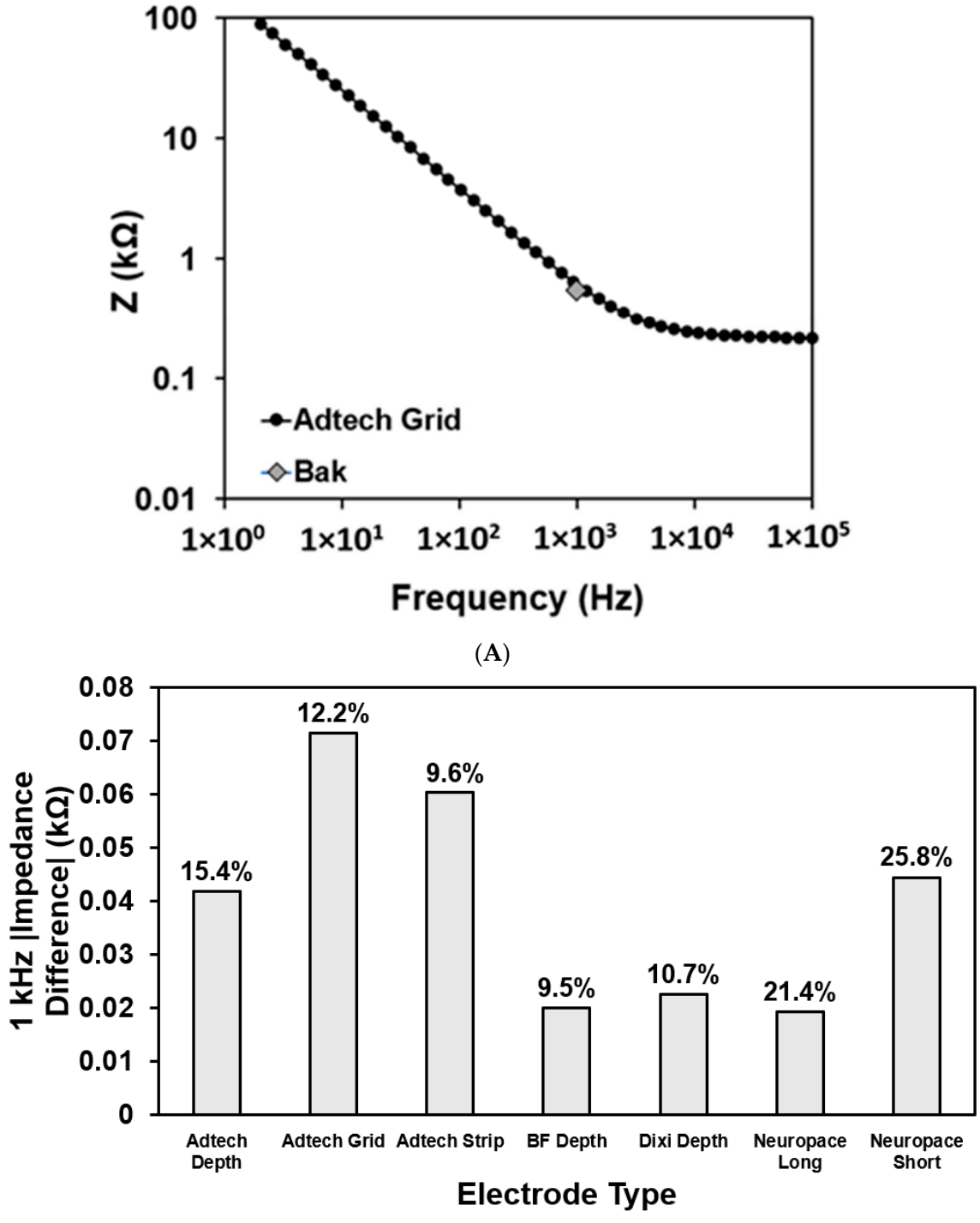

Figure 6. Comparison of single-frequency (1 kHz) impedance measurements conducted using the Bak Electrode Impedance Tester and Palmsens4 Potentiostat. (**A**) Plot of impedance measured via PalmSens4 Potentiostat (black dots) and Bak Electrode Impedance Tester (Gray). (**B**) Bar plots showing the difference in 1 kHz impedance measured between the PalmSens device and Bak Electrode Impedance tester. To obtain an impedance value at 1 kHz for PalmSens, we interpolated adjacent frequency (1.2 kHz, 0.9 kHz) impedance values. A larger percentage means a greater percentage difference between PalmSens and Bak impedance recordings. Note that the measurement resolution of the Bak impedance tester was 50 ohms, so repeated measures did not produce sufficient variance to produce error bars.

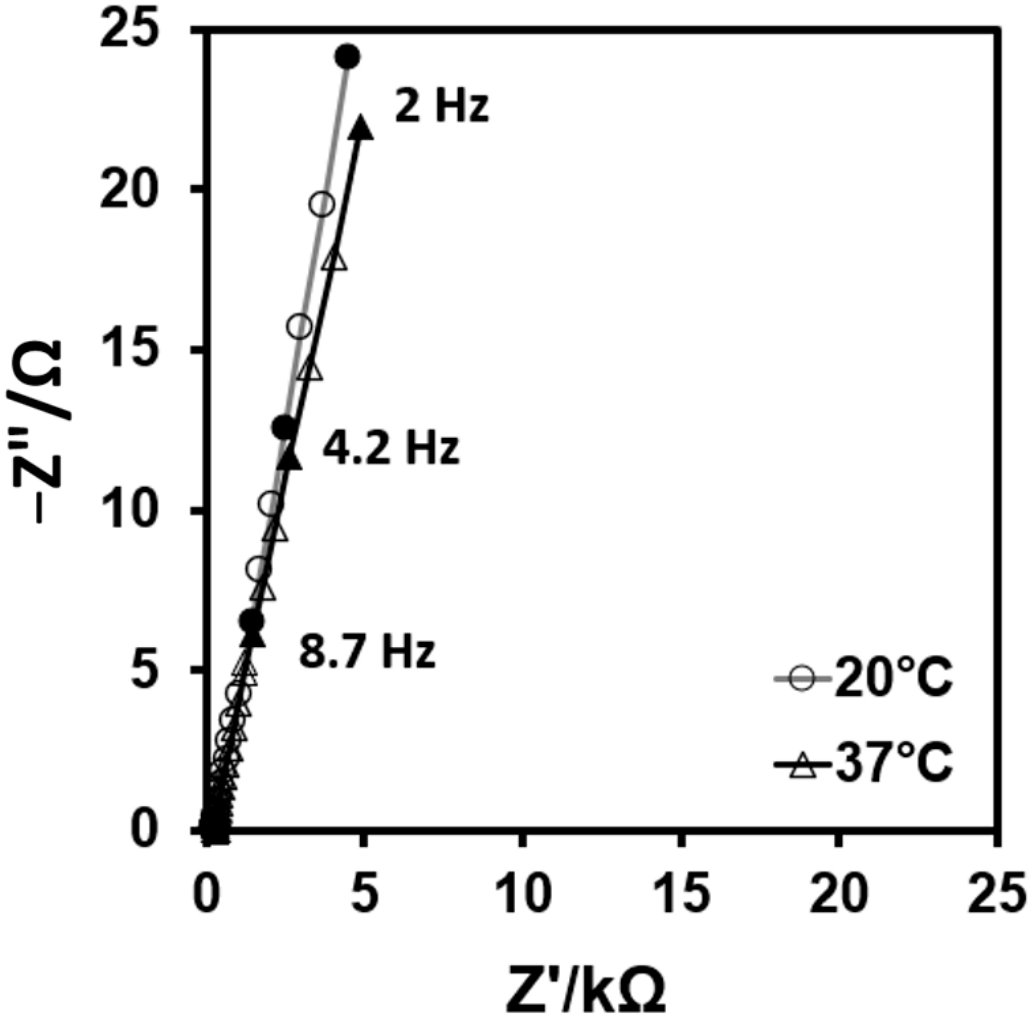

Figure 7. Comparison of EIS data collected using an Ad-Tech SEEG depth lead (RD10R-SP05X-000) at two temperature points, with all other parts of the system being identical. Note that the lower temperature (20 °C) produced a distinctly different result from the higher temperature (37 °C), with differences being particularly apparent at lower frequencies (towards top-right section of graph).

4.6. Counter Electrode Materials

Several counter electrode types are included in our dataset to illustrate the impact of electrode selection on EIS results. In typical in vitro applications, an electrode of similar material to the working electrode, with the highest possible surface area, is preferred. As all of our working electrode materials consisted of platinum–iridium alloys, platinum counter electrodes are preferred. We tested both a platinum wire (7.5 cm length, 0.5 mm diameter, 1178 mm^2 surface area) and platinum foil (2500 mm^2 surface area) (Figure 8). For in vivo measurements, a titanium screw (61 mm^2 surface area) embedded within the animal's dental acrylic cephalic implant served as a counter electrode, contacting the dural surface. A similar titanium screw was also tested in vitro, shown in Figure 8 for comparison purposes. Note the distinct differences in measurements obtained with the screw, highlighting some limitations of collecting data in vivo. All comparison measurements in Figure 8 were performed with identical parameters aside from the chosen counter/reference electrode.

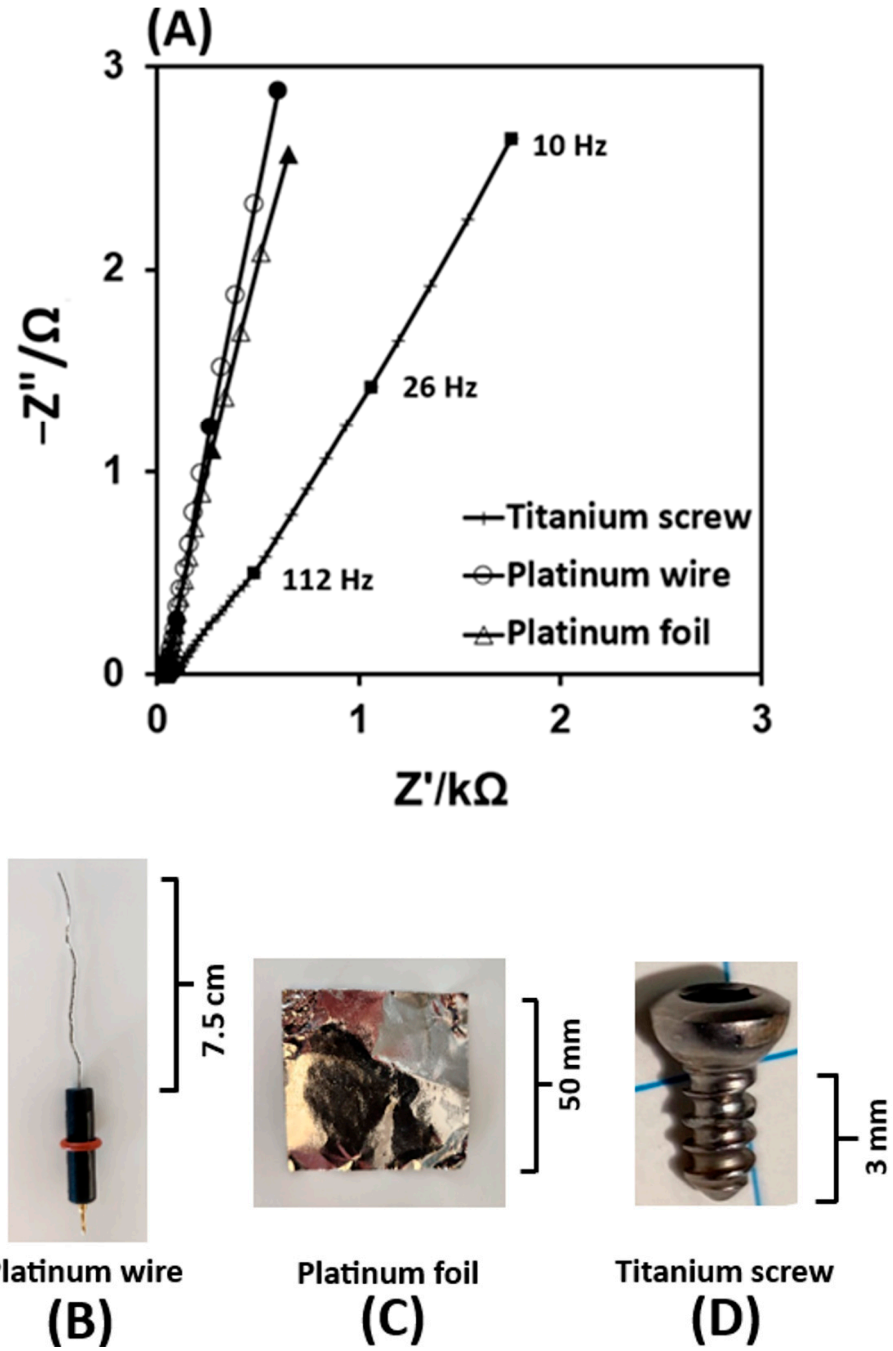

Figure 8. Comparison of differences in impedance spectra collected using various counter/reference electrodes. (**A**) Comparison of EIS data collected with an Ad-Tech EEG depth lead (RD10R-SP05X-000) as the working electrode, using three different counter-electrodes. These data were collected in a two-electrode configuration in phosphate-buffered saline at a regulated temperature of 37 °C. (**B**) The platinum wire electrode with a 7.5 cm length, 0.5 mm diameter, and 1178 mm^2 surface area. (**C**) 50 × 50 mm platinum foil electrode with a 2500 mm^2 surface area. (**D**) Titanium screw used in vivo as a counter/reference electrode. An identical screw was used for the in vitro comparison shown in (**A**). Both screws' cylindrical barrels had an approximate 61 mm^2 surface area.

Author Contributions: K.P.O. and B.J.P. performed experimental design, data acquisition, error analysis/modeling, writing, and figure creation. All remaining authors contributed equally to study design/conceptualization, writing, and technical validation. All authors have read and agreed to the published version of the manuscript.

Funding: This research was funded by NIH grant number R01 NS111019.

Institutional Review Board Statement: The animal study protocol was approved by the Institutional Animal Care and Use Committee of Weil Cornell Medical College (protocol code 2010-0122, date 13 March 2011).

Data Availability Statement: Data discussed here can be found on the Dryad repository at the following link: https://doi.org/10.5061/dryad.8931zcrvw, accessed on 9 April 2024.

Acknowledgments: Animal work included in this dataset was performed at the Brain and Mind Research Institute, Weil Cornell Medicine, New York, New York.

Conflicts of Interest: There are no conflicts of interest to declare for the work included in this manuscript.

Abbreviations

aCSF	Artificial cerebrospinal fluid
C	Counter electrode
CPE	Constant phase element
CSV	Comma-separated values (file format)
DBS	Deep brain stimulation
ECoG	Electrocorticography
EIS	Electrochemical impedance spectroscopy
ETI	Electrode–tissue interface
IACUC	Institutional Animal Care and Use Committee
NHP	Nonhuman primate
PBS	Phosphate-buffered saline
SNR	Signal-to-noise ratio
R	Reference rlectrode
RARC	Research Animal Resource Center
W	Working electrode

References

1. Butson, C.R.; McIntyre, C.C. Tissue and electrode capacitance reduce neural activation volumes during deep brain stimulation. *Clin. Neurophysiol.* **2005**, *116*, 2490–2500. [CrossRef]
2. Cui, J.; Mivalt, F.; Sladky, V.; Kim, J.; Richner, T.; Lundstrom, B.; Gompel, J.V.; Wang, H.; Miller, K.; Gregg, N. Acute to long-term characteristics of impedance recordings during neurostimulation in humans. *J. Neural Eng.* **2024**, *21*, 026022. [CrossRef]
3. Sillay, K.A.; Ondoma, S.; Wingeier, B.; Schomberg, D.; Sharma, P.; Kumar, R.; Miranpuri, G.S.; Williams, J. Long-Term Surface Electrode Impedance Recordings Associated with Gliosis for a Closed-Loop Neurostimulation Device. *Ann. Neurosci.* **2019**, *25*, 289–298. [CrossRef]
4. Stacey, W.C.; Kellis, S.; Patel, P.R.; Greger, B.; Butson, C.R. Signal distortion from microelectrodes in clinical EEG acquisition systems. *J. Neural Eng.* **2012**, *9*, 056007. [CrossRef] [PubMed]
5. Cassar, I.R.; Yu, C.; Sambangi, J.; Lee, C.D.; Whalen, J.J.; Petrossians, A.; Grill, W.M. Electrodeposited platinum-iridium coating improves in vivo recording performance of chronically implanted microelectrode arrays. *Biomaterials* **2019**, *205*, 120–132. [CrossRef] [PubMed]
6. Polikov, V.S.; Tresco, P.A.; Reichert, W.M. Response of brain tissue to chronically implanted neural electrodes. *J. Neurosci. Methods* **2005**, *148*, 1–18. [CrossRef]
7. Cody, P.A.; Eles, J.R.; Lagenaur, C.F.; Kozai TD, Y.; Cui, X.T. Unique electrophysiological and impedance signatures between encapsulation types: An analysis of biological Utah array failure and benefit of a biomimetic coating in a rat model. *Biomaterials* **2018**, *161*, 117–128. [CrossRef]
8. McConnell, G.C.; Rees, H.D.; Levey, A.I.; Gutekunst, C.A.; Gross, R.E.; Bellamkonda, R.V. Implanted neural electrodes cause chronic, local inflammation that is correlated with local neurodegeneration. *J. Neural Eng.* **2009**, *6*, 056003. [CrossRef]
9. Otto, K.J.; Johnson, M.D.; Kipke, D.R. Voltage pulses change neural interface properties and improve unit recordings with chronically implanted microelectrodes. *IEEE Trans. Biomed. Eng.* **2006**, *53*, 333–340. [CrossRef]
10. Straka, M.M.; Shafer, B.; Vasudevan, S.; Welle, C.; Rieth, L. Characterizing longitudinal changes in the impedance spectra of in-vivo peripheral nerve electrodes. *Micromachines* **2018**, *9*, 587. [CrossRef]

11. Williams, J.C.; Hippensteel, J.A.; Dilgen, J.; Shain, W.; Kipke, D.R. Complex impedance spectroscopy for monitoring tissue responses to inserted neural implants. *J. Neural Eng.* **2007**, *4*, 410–423. [CrossRef] [PubMed]
12. Lempka, S.F.; Miocinovic, S.; Johnson, M.D.; Vitek, J.L.; McIntyre, C.C. In vivo impedance spectroscopy of deep brain stimulation electrodes. *J. Neural Eng.* **2009**, *6*, 046001. [CrossRef] [PubMed]
13. Kane, S.R.; Cogan, S.F.; Ehrlich, J.; Plante, T.D.; McCreery, D.B.; Troyk, P.R. Electrical performance of penetrating microelectrodes chronically implanted in cat cortex. *IEEE Trans. Biomed. Eng.* **2013**, *60*, 2153–2160. [CrossRef] [PubMed]
14. Orazem, M.E.; Tribollet, B. An integrated approach to electrochemical impedance spectroscopy. *Electrochim. Acta* **2008**, *53*, 7360–7366. [CrossRef]
15. Franks, W.; Schenker, I.; Schmutz, P.; Hierlemann, A. Impedance characterization and modeling of electrodes for biomedical applications. *IEEE Trans. Biomed. Eng.* **2005**, *52*, 1295–1302. [CrossRef] [PubMed]
16. Lasia, A. The Origin of the Constant Phase Element. *J. Phys. Chem. Lett.* **2022**, *13*, 580–589. [CrossRef] [PubMed]
17. Schiavone, G.; Kang, X.; Fallegger, F.; Gandar, J.; Courtine, G.; Lacour, S.P. Guidelines to Study and Develop Soft Electrode Systems for Neural Stimulation. *Neuron* **2020**, *108*, 238–258. [CrossRef] [PubMed]
18. Boehler, C.; Carli, S.; Fadiga, L.; Stieglitz, T.; Asplund, M. Tutorial: Guidelines for standardized performance tests for electrodes intended for neural interfaces and bioelectronics. *Nat. Protoc.* **2020**, *15*, 3557–3578. [CrossRef]
19. Wang, S.; Zhang, J.; Gharbi, O.; Vivier, V.; Gao, M.; Orazem, M.E. Electrochemical impedance spectroscopy. *Nat. Rev. Methods Primers* **2021**, *1*, 41. [CrossRef]
20. Vivier, V.; Orazem, M.E. Impedance Analysis of Electrochemical Systems. *Chem. Rev.* **2022**, *122*, 11131–11168. [CrossRef]
21. O'Sullivan, K.P.; Philip, B.J.; Baker, J.L.; Orazem, M.E.; Otto, K.J.; Butson, C.R. In vivo and in vitro electrochemical impedance spectroscopy analysis of acute and chronic intracranial electrodes. *Dryad*. [CrossRef]
22. Sluyters-Rehbach, M. International Union of Pure and Applied Chemistry Physical Chemistry Division Commission on Electrochemistry* Impedances of Electrochemical Systems: Terminology, Nomenclature and Representation Part I: Cells with Metal Electrodes and Liquid Solutions (IUPAC Recommendations 1994). 1994, pp. 1831–1891. Available online: https://www.degruyter.com/document/doi/10.1351/pac199466091831/html?lang=en (accessed on 9 April 2024).
23. Baker, J.L.; Ryou, J.-W.; Wei, X.F.; Butson, C.R.; Schiff, N.D.; Purpura, K.P. Robust modulation of arousal regulation, performance, and frontostriatal activity through central thalamic deep brain stimulation in healthy nonhuman primates. *J. Neurophysiol.* **2016**, *116*, 2383–2404. [CrossRef] [PubMed]
24. McCann, H.; Pisano, G.; Beltrachini, L. Variation in Reported Human Head Tissue Electrical Conductivity Values. *Brain Topogr.* **2019**, *32*, 825–858. [CrossRef] [PubMed]
25. Azizollahi, H.; Aarabi, A.; Wallois, F. Effects of uncertainty in head tissue conductivity and complexity on EEG forward modeling in neonates. *Hum. Brain Mapp.* **2016**, *37*, 3604–3622. [CrossRef] [PubMed]
26. Watson, W.; Orazem, M.E. EIS: Measurement Model Program program, Version 1.8. *ECSarXiv* **2023**. [CrossRef]
27. Shukla, P.K.; Orazem, M.E.; Crisalle, O.D. Validation of the measurement model concept for error structure identification. *Electrochim. Acta* **2004**, *49*, 2881–2889. [CrossRef]
28. Carson, S.L.; Orazem, M.E.; Crisalle, O.D.; García-Rubio, L. On the Error Structure of Impedance Measurements. *J. Electrochem. Soc.* **2003**, *150*, E477. [CrossRef]
29. Brachman, M.K.; Macdonald, J.R. Generalized immittance kernels and the Kronig–Kramers relations. *Physica* **1956**, *22*, 141–148. [CrossRef]
30. Jakšić, M.M.; Newman, J. The Kramers–Kronig Relations and Evaluation of Impedance for a Disk Electrode. *J. Electrochem. Soc.* **1986**, *133*, 1097–1101. [CrossRef]
31. Brug, G.J.; Eeden ALG van den Sluyters-Rehbach, M.; Sluyters, J.H. The analysis of electrode impedances complicated by the presence of a constant phase element. *J. Electroanal. Chem. Interfacial Electrochem.* **1984**, *176*, 275–295. [CrossRef]
32. Orazem, M.E.; Pébère, N.; Tribollet, B. Enhanced Graphical Representation of Electrochemical Impedance Data. *J. Electrochem. Soc.* **2006**, *153*, B129. [CrossRef]
33. Badstübner, K.; Stubbe, M.; Kröger, T.; Mix, E.; Gimsa, J. Impedance detection of the electrical resistivity of the wound tissue around deep brain stimulation electrodes permits registration of the encapsulation process in a rat model. *J. Electr. Bioimpedance* **2017**, *8*, 11–24. [CrossRef]